

Unlocking cell chemistry evolution with operando fibre optic infrared spectroscopy in commercial Na(Li)-ion batteries

Received: 30 May 2022

Accepted: 14 September 2022

 Check for updates

C. Gervill  -Mouravieff^{1,2}, C. Boussard-Pl  del³, Jiaqiang Huang^{1,2,4},
C. Leau^{1,2}, L. Albero Blanquer^{1,2,5}, M. Ben Yahia⁶, M.-L. Doublet⁶,
S. T. Boles⁷, X. H. Zhang³, J. L. Adam³ & J.-M. Tarascon^{1,2,5} ✉

Improvements to battery performance, reliability and lifetime are essential to meet the expansive demands for energy storage. As part of this, continuous monitoring of the dynamic chemistry inside cells offers an exciting path to minimizing parasitic reactions and maximizing sustainability. Building upon recent fibre-optic/battery innovations, we report the use of operando infrared fibre evanescent wave spectroscopy to monitor electrolyte evolution in 18650 Na-ion and Li-ion cells under real working conditions. This approach enables identification of chemical species and reveals electrolyte and additive decomposition mechanisms during cycling, thereby providing important insights into the growth and nature of the solid–electrolyte interphase, the dynamics of solvation and their complex interrelations. Moreover, by directly embedding fibres within the electrode material, we demonstrate simultaneous observations of both the material structural evolution and the Na(Li) inventory changes upon cycling. This illuminating sensing method has the power to reveal the otherwise opaque chemical phenomena occurring within each key battery component.

Batteries play a central role in the ongoing transition from fossil fuels to renewable energy and are the versatile key enablers for the deployment of electric transportation, but their full acceptance is highly reliant on the ability of scientists to improve their autonomy, cost, lifetime and safety¹. Since chemical and electrochemical reactions are dynamical processes, these ‘living’ devices suffer from multi-parameter degradation mechanisms leading, for instance, to the formation of the solid–electrolyte interphase (SEI), which often governs the life of the cell. Consequently, monitoring the intertwined electrolyte decomposition and SEI evolution is of paramount importance to understanding and controlling the battery lifetime and safety. While operando techniques such as nuclear magnetic resonance (NMR), transmission electron

microscopy, infrared (IR) or electron paramagnetic resonance are powerful tools to access the microscopic scale^{2–5}, they are not readily translated out of laboratory test cells and into commercial-grade batteries. In this context, non-destructive diagnostic techniques, such as optical sensing, allow for real-time characterization with spatial resolution afforded by placing sensors directly inside cells^{6,7}. Using optical fibre Bragg grating (FBG) sensors, numerous parameters of interest can be measured, such as temperature (*T*), pressure (*P*) and strain (ϵ), with the feasibility of correlating these metrics to battery electrochemical behaviour^{8,9}.

Moreover, using multiple sensors, we have even succeeded in tracking the heat associated with the formation of the SEI¹⁰ and its

¹Chimie du Solide et de l’Energie, Coll  ge de France, Paris, France. ²R  seau sur le Stockage Electrochimique de l’Energie (RS2E), Amiens, France. ³Institut des Sciences Chimiques de Rennes (ISCR), Univ. Rennes, CNRS, Rennes, France. ⁴Sustainable Energy and Environment Thrust, The Hong Kong University of Science and Technology (Guangzhou), Guangzhou, China. ⁵Sorbonne Universit  –Universit   Pierre-et-Marie-Curie Paris (UPMC), Paris, France. ⁶Institute Charles Gerhardt of Montpellier (ICGM), Univ. Montpellier, CNRS, ENSCM, Montpellier, France. ⁷Department of Energy and Process Engineering, Faculty of Engineering, Norwegian University of Science and Technology (NTNU), Trondheim, Norway. ✉e-mail: jean-marie.tarascon@college-de-france.fr

dynamic evolution during cycling¹¹. Although prolific, such approaches are ill-suited to capturing molecular insights occurring within each critical component of the battery, and the cascade of chemical reactions underlying the formation of the SEI. Aiming to close this gap, tilted FBG sensors offer a possibility for accessing additional observables (refractive index and turbidity), since by their nature, they allow for fibre-guided light to interact with its local surroundings¹². However, these sensors are still not capable of identifying individual molecular species.

Possible ways to overcome this limitation can be inspired by the field of spectroscopy and the use of UV–visible, IR and Raman activity ranges for chemical detection^{13–15}. For instance, photonic crystal fibres are widely used in the development of biosensors for molecular recognition^{16,17} and, once paired with microfluidics, have recently been employed in the field of batteries to follow the evolution of an electrolyte by Raman spectroscopy during cycling¹⁸. However, a weakness of the reported work is that it hinges on an external system (for example, pumps and piping), preventing both continuous monitoring and the ability to track changes in the electrode materials themselves. Looking for other inspiration, we came across the use of fibre-based IR spectroscopy in the medical field^{19–21}. Interestingly, even though this *ex vivo* approach can detect and follow severe liver disease via the detection of specific molecules, such an approach has never been implemented with battery electrolytes or electrodes under real test conditions, where electrochemical potentials and reactive chemistries continually pose complex challenges.

Herein, we report in operando IR fibre evanescent wave spectroscopy (FEWS) in commercial 18650 Na-ion cells and in Swagelok-type Li(Na)-ion cells. Since silica (SiO₂) optical fibres commonly employed in telecommunications are restricted to the 0.8 to 2 μm transmission region, we instead implement chalcogenide (sulfides, selenides, tellurides) glass fibres, which have transmission windows ranging from 3 to 13 μm ²². This opens a critical pathway to molecular identification and monitoring of the chemical dynamics occurring inside a cell during cycling. Hence, the method can provide evidence of the steps involved for SEI growth after cell manufacturing, as well as a means for tracking the Li(Na) inventory upon cycling (for example, state of charge and state of health) and corresponding ion insertion kinetics. Such revelations highlight the emergence of a new era for rechargeable batteries, both in terms of chemical selection and cycling conditions.

Operando IR fibre evanescent wave spectroscopy

Figure 1a shows the experimental set-up for conducting fibre optic infrared detection via the use of Te₂As₃Se₅ (TAS) fibre. As depicted, absorption spectroscopy relies on the use of evanescent waves to probe molecular species at the fibre surface over a distance that depends upon the refractive index of the surrounding media (calculation in Supplementary Fig. 1). Typical experiments are realized by passing the TAS fibre through a pre-drilled 18650 jelly roll cell for the case of Na-ion (Na₃V₂(PO₄)₂F₃/hard-carbon (NVPF/HC)) chemistry (Fig. 1a), or across a modified Swagelok cell (as described in the Fig. 1b,c caption). The cells can then be connected to a Fourier transform infrared spectrometer equipped with a mercury–cadmium–tellurium detector that collects IR-FEWS spectra while the cell is charged and discharged.

As a proof of concept, operando IR spectra recorded on a modified Swagelok cell (Fig. 1c) before and after adding the electrolyte are shown in Fig. 2a, and compared with reference spectra of the same solutions acquired with attenuated total reflectance spectroscopy (Fig. 2b). As expected, no absorbance is observed in the absence of electrolyte (considering the absorbance $A = \log\left(\frac{I_0}{I_s}\right)$ and $I_s = I_0$, with I_0 and I_s the transmitted intensity through the fiber with and without the sample, respectively). By contrast, at each injection step, the IR bands characteristic of the added solutions appear concomitantly to their

injection in the cell (Fig. 2a). This first result validates the use of TAS fibres to characterize electrolytes with a high molecular sensitivity (concentration less than 1%; Supplementary Fig. 2) and fast response (4 seconds).

Pure electrolyte mixture

Before conducting operando measurements in 18650 cells, a few considerations on the reliability of the measurement needed to be addressed. First, since the refractive index is a function of temperature, temperature will affect the penetration depth of the evanescent wave and hence the absorbance. Therefore it was essential to determine if temperature could affect our results, while bearing in mind the range of temperature changes that can occur during battery cycling (Supplementary Figs. 3 and 4). With a temperature change of 5 °C, the measured change in signal absorbance is 1% and the shifts in band positions are less than the spectrometer resolution; thus we can safely neglect any temperature effect in exploiting future IR-FEWS data. Second, TAS fibres were installed into commercial NVPF/HC 18650 Na-ion cells, and the inertness of the IR fibre was checked by monitoring the capacity retention of two cells with and without hosting fibres and by leaving the fibres in the electrolyte at 55 °C for one month (Supplementary Figs. 5 and 6). Both cells show the same capacity retention at least up to 100 cycles, while scanning electron microscopy observations of the fibre stored in a harsh environment do not reveal any concerning visible change in fibre morphologies. Altogether, these results indicate that the nature of the fibre, together with the means of injecting it into the cell, have no discernable impact on the electrochemical process nor any interaction with the cell environment.

Having done these tests, we were ready to explore the potential of our optical IR-FEWS technique in a NVPF/HC 18650 cell with 1 M NaPF₆ in dimethyl carbonate (NaPF₆/DMC) electrolyte, which is known to be a mildly unstable system. In addition to the TAS fibre, a FBG sensor was incorporated in the cell to measure the internal temperature changes (ΔT) during cycling. The detailed working principle and calibration curves of the FBG are given in Supplementary Fig. 7.

The cycling data shown in Fig. 3a indicate an initial irreversibility as high as 80 mAh g_{NVPF}⁻¹ between the first charge and discharge (-160 mAh g_{NVPF}⁻¹ and 80 mAh g_{NVPF}⁻¹ capacities, respectively) indicative of copious electrolyte decomposition, in concert with a large temperature increase during the charge. To spot changes only in the cell's evolving chemistry, the IR-FEWS absorbance spectra together with the relative evolution of absorbance $A(t)-A(t_0)$, after subtracting from the absorbance spectra $A(t)$ the absorbance spectra at $t = 0$ ($A(t_0)$) when the cell is first connected, were plotted (Fig. 3b–d).

During the first charge, a colour change from green to dark blue is observed in Fig. 3b and is ascribed to the decrease of DMC absorption bands (Supplementary Fig. 8 for DMC and NaPF₆/DMC reference spectra), while at a higher voltage, the change from green to yellow highlights the formation of products, confirming the expected decomposition of DMC. Turning to absorbance as a function of wavenumber (Fig. 3d), we find that most of the bands corresponding to decomposition (negative band) and species formation (positive band) evolve during the first charge and can be attributed, according to the literature, to free and coordinated DMC, labelled DMC_{free} and DMC_{coord}, respectively (Fig. 3c,d)²³. Indeed, the solvation of Na⁺ ions by the DMC molecules translates to a weakening of the C=O vibrational band of DMC, resulting in a shift from 1,753 cm⁻¹ to 1,732 cm⁻¹ and in a strengthening of the O–C–O band, associated with a shift from 1,274 cm⁻¹ to 1,315 cm⁻¹ (Supplementary Fig. 8).

Interestingly, Fig. 3e highlights the asymmetric changes in the amplitude ratio of the free and solvated bands of DMC. This effect can be visualized within the $\nu\text{C=O}$ absorption domain between 1,700 cm⁻¹ and 1,800 cm⁻¹ with the appearance of two peaks evolving in opposite directions: the positive shift, corresponding to the relative absorbance band of free DMC, has a smaller amplitude compared to the negative

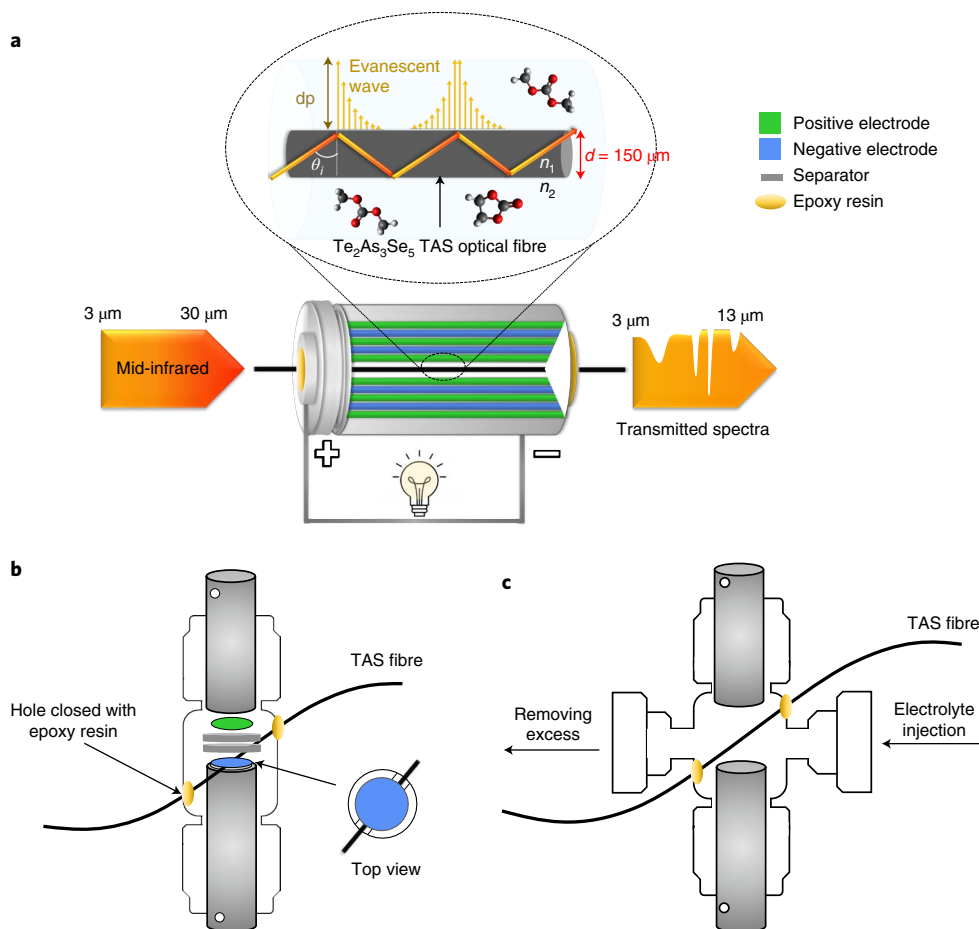


Fig. 1 | Integration of chalcogenide fibre into batteries. **a**, Schematic drawing of mid-infrared light in the range from 830 to 5,000 cm^{-1} propagating via internal reflections through the TAS fibre core (fibre diameter, $d = 150 \mu\text{m}$). At the fibre surface, an evanescent wave is created, whose depth of penetration (dp , $\sim 1 \mu\text{m}$) is given by the relation $dp = \frac{\lambda}{2\pi\sqrt{n_1^2 \sin^2 \theta_i - n_2^2}}$, where λ is the wavelength of the propagating light, θ_i is the incident angle of the light and n_1 and n_2 are the refractive indexes of the fibre and of its surrounding medium, respectively. The TAS fibre is passing through the central void of a 18650 jelly roll allowing IR-FEWS

operando measurements of the electrolyte while cycling the battery.

b, Two-electrode Swagelok cell modified for operando measurements. The body of the cell has been drilled with two holes so that the fibre can be embedded in the electrode material. **c**, Modified two-electrode Swagelok cell for acquisition of reference spectra. The Swagelok cell is drilled with two holes for the fibre to pass through, and two metal tubes terminated with rubber septa are welded to the cell body to inject solutions using syringes and evacuate the electrolyte while maintaining the inert atmosphere inside the cell core.

band shift, corresponding to coordinated DMC. A similar effect is visible between 1,150 cm^{-1} and 1,400 cm^{-1} corresponding to the vOCO band of free and coordinated DMC. This indirectly indicates electrolyte dissolution involving both salt and solvent, which is confirmed by the decrease of the vPF band at 850 cm^{-1} starting at the beginning of the charge and reaching a stable value before the end of charge (Fig. 3e and ex situ spectra in Supplementary Fig. 9). The vPF band no longer changes upon subsequent cycling or when the cell is left under an open circuit voltage (Supplementary Fig. 10), which indicates a partial, but irreversible, decomposition of NaPF₆ that is fully consistent with the presence of F⁻-based components (for example, NaF) in the SEI, consistent with previously demonstrated X-ray photoelectron spectroscopy experiments on a similar NVPF/HC cell chemistry²⁴.

Besides these bands, we observe a broad band between 1,600 cm^{-1} and 1,700 cm^{-1} (indicated by a black dotted line in Fig. 3c,d) that grows upon charging and that could reasonably be assigned to the CO₂ asymmetric stretching mode of alkyl carbonate (RCOO⁻). The large band width and low amplitude of the band are explained by the poor solubility of alkyl carbonate in NaPF₆/DMC (Supplementary Fig. 11). This confirms the well-known reacting pathway of electrochemical reduction of DMC^{25,26} that can proceed via the cleaving of either the C–O or O–CH₃

bonds, leading to alkyl carbonate and methoxy species, respectively. The absence of evidence of bands associated with Na–methoxy in our experiment may indicate that one bond cleavage is favoured over the other under our experimental conditions.

Binary electrolyte mixture

We now test the reliability of our technique by exploring a 18650 NVPF/HC cell containing a binary electrolyte mixture (1 M NaPF₆ in ethylene carbonate (EC)/DMC (1:1, v/v)). Its capacity is shown in Fig. 4a together with the temperature evolution, revealing three peaks during the first charge and two peaks during the following discharge, in perfect agreement with our previous work¹⁰ in which we correlated the larger temperature peak to electrolyte decomposition and SEI formation. The IR-FEWS absorbance spectra and relative absorbance $A(t)-A(t_0)$ plots are given in Fig. 4b–d, with EC bands assigned according to reference spectra (Supplementary Fig. 8) and from previous studies²⁷. Interestingly, the relative change in the IR contour plot (Fig. 4b) from blue to yellow confirms the formation of extra species with the appearance of several bands in the $A(t)-A(t_0)$ relative absorbance spectra (Fig. 4d).

The growth of these bands upon charge (indicated by purple stars) can be attributed to the dimethyl-2,5-dioxa-hexane carboxylate

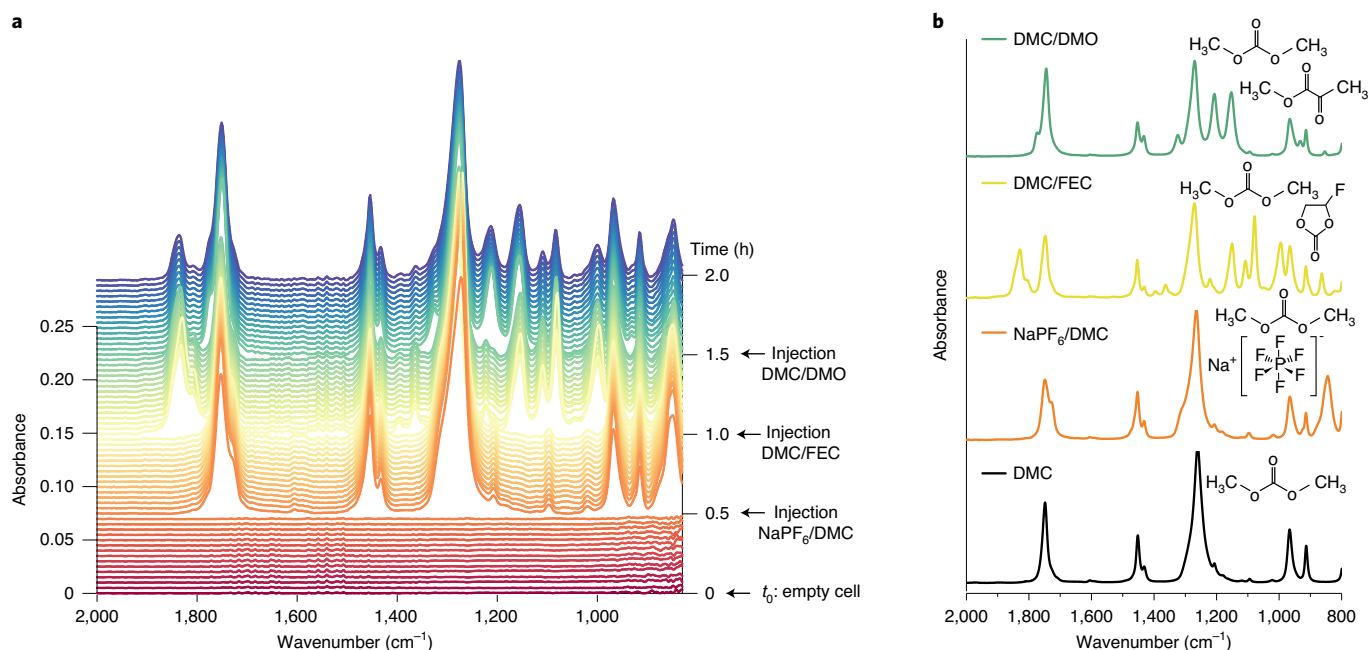


Fig. 2 | Online IR-FEWS measurement. **a**, IR-FEWS absorbance spectra as a function of time, obtained via the use of a modified two-electrode Swagelok cell for hosting the TAS fibre. The IR-FEWS absorbance spectra were recorded every 120 s with a resolution of 4 cm^{-1} , a number of scans of 16 and an acquisition time of 4 s. The acquisition starts at $t = 0$ when the cell is empty; then every 30 minutes,

different solutions are added in the following order: 1 M NaPF_6 in DMC (NaPF_6/DMC), DMC and fluoroethylene carbonate (1:1, v/v, DMC/FEC) and DMC saturated with dimethyl oxalate (DMC/DMO). **b**, Reference IR-attenuated total reflectance spectroscopy absorbance spectra of the different solutions injected during the experiment.

(DMDOHC) resulting from the well-known transesterification reaction between EC and DMC^{25,28}. The DMDOHC bands' absorption peaks reach their maximum amplitudes at the end of the charging (and beginning of discharging—most likely due to incomplete reaction and delays in species diffusion) and then stabilize on the subsequent discharge (Fig. 4e), suggesting their participation in the formation of the SEI that is nearly completed at the first charge. In concert, the decrease of the $\nu\text{C}=\text{O}$ band of EC at $1,775\text{ cm}^{-1}$ (yellow circle) and the subsequent DMDOHC bands' growth confirm the EC's involvement in SEI formation (Fig. 4e).

Interestingly, the $\nu\text{C}=\text{O}$ band of DMC is visible all along the charge process, although it may be partly hidden by the DMDOHC bands, proving the ability of EC to prevent DMC decomposition; this is in line with the fact that the solvent with the highest dielectric constant, EC, will decompose first.

As observed for the NaPF_6/DMC electrolyte, the $\nu\text{P}-\text{F}$ band at 850 cm^{-1} decreases during the first charge and stabilizes during discharge (Fig. 4e). In parallel, note the decrease and increase of the bands corresponding to the $\nu\text{C}-\text{C}$ vibration of the coordinated ($1,180\text{ cm}^{-1}$) and uncoordinated ($1,164\text{ cm}^{-1}$) EC ring, as expected due to the change in the salt concentration, associated with the degradation of NaPF_6 (Fig. 4e). Because of the Fermi resonance of the EC molecule²⁹, this effect cannot be detected on the $\nu\text{C}=\text{O}$ band stretching, but is confirmed by observing the solvation changes on the IR spectra of solutions at different concentrations of salt in EC/DMC, as shown in Supplementary Fig. 12. Finally, the broad band growth observed at $1,675\text{ cm}^{-1}$ most probably pertains to a sodium alkyl carbonate, and the one at $1,033\text{ cm}^{-1}$, to sodium methoxide (indicated by the black dotted line in Fig. 4c,d)³⁰. However, the weak intensity of these bands together with their broadness does not allow a precise identification. This appearance of several new species in the electrolyte can be explained by the poor solubility of alkoxides and carbonates in DMC, as opposed to EC/DMC (Supplementary Fig. 11), which is consistent with the greater dielectric constant of EC ($\epsilon_r = 89.7$) compared to DMC ($\epsilon_r = 3.1$).

Decomposition of vinylene carbonate additive

As a proof of concept, the decomposition of the vinylene carbonate (VC) additive was studied in NVPF/HC 18650 cells with 1 M NaPF_6 in EC/DMC (1:1, v/v) electrolyte with 3 wt% VC for two cycles at a C/5 rate (Fig. 5a). Reference spectra of VC and 1 M NaPF_6 in EC/DMC plus 3 wt% VC are given in Supplementary Fig. 13 for comparison. The contour plot of the relative absorbance evolution, $A(t)-A(t_0)$ shown in Fig. 5b indicates that most of the chemical evolution occurs during the first charge and stabilizes thereafter, in agreement with an important increase of the cell temperature, observed only during the first charge (Fig. 5a).

The IR absorbance spectra and their relative evolution $A(t)-A(t_0)$ are presented in Fig. 5b–d. The decomposition of VC is evidenced by the decrease in intensity of its band at $1,834\text{ cm}^{-1}$ (Fig. 5e, bottom), corresponding to the $\nu\text{C}=\text{O}$ stretching mode (black dotted line in Fig. 5c,d). Concomitantly, the derivative capacity dQ/dV shows the onset of a broad peak at 3.1 V during the first charge (Fig. 5e, top) that can be unambiguously ascribed to VC decomposition in light of previous studies on Na-ion NVPF/HC cells²⁴ and that matches perfectly with the largest peak in the thermal profile (Fig. 5e, middle). The $\nu\text{C}=\text{O}$ band of VC decays during the charge, prior to reaching a plateau at the end of the first charge (Fig. 5f). The absorbance of the $\nu\text{C}=\text{O}$ band remains nearly constant upon the subsequent discharge and the following cycles, and the absence of any peak in the dQ/dV plot for the second charge confirms the general belief that VC contributes to the formation of a stable SEI during the first charge through the formation of an elastomer that prevents further electrolyte decomposition³¹. Interestingly, and in contrast to the previous case of binary mixtures, none of the characteristic bands of DMDOHC ($1,258\text{ cm}^{-1}$) or sodium carbonate ($1,675\text{ cm}^{-1}$) are detected, thus demonstrating the effectiveness of the additive³².

In addition to the evolution of the VC bands upon charging, changes in the $\nu\text{C}=\text{O}$ bands of free EC ($1,799\text{ cm}^{-1}$) and free DMC ($1,749\text{ cm}^{-1}$) are consistent with an overall decrease of PF_6^- in the electrolyte. As with the previous cases, the PF_6^- anion decomposes with an

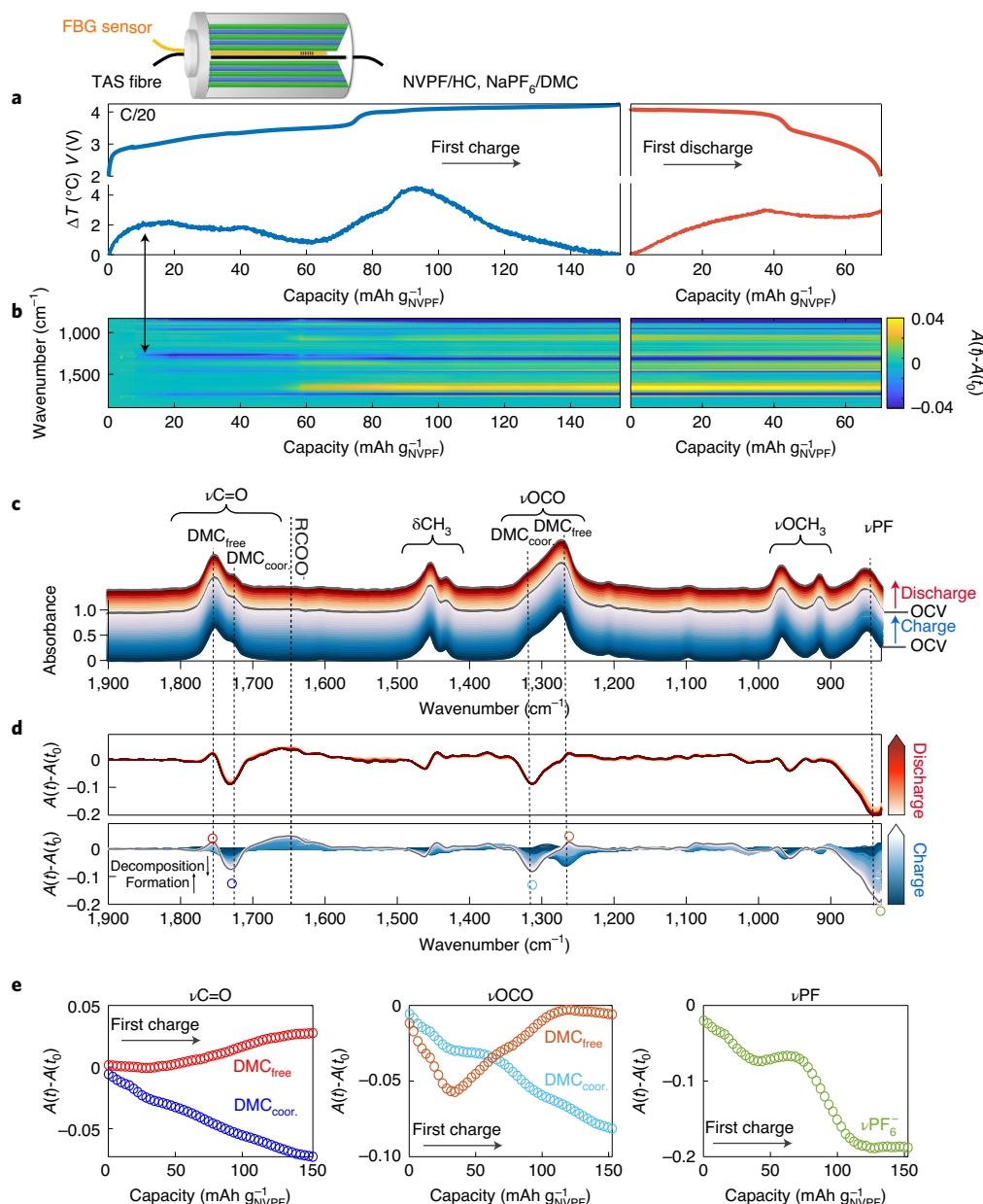


Fig. 3 | Operando IR-FEWS measurements of NaPF₆/DMC decomposition in 18650. a, Voltage (top) and temperature change (bottom) during the first charge (blue) and discharge (red) of a NVPF/HC 18650 cell with NaPF₆/DMC electrolyte at C/20. **b,** Wavenumber versus capacity contour plot of the IR-FEWS operando absorbance spectra. The colour change from green to yellow or blue implies a change in the relative evolution of absorbance $A(t)-A(t_0)$, as showed in the colour bar. **c,** Operando IR-FEWS spectra collected during the first charge with the colours of the spectra varying from blue in charge to red in discharge. Spectra collected during open circuit voltage (OCV) are coloured in grey. The notations DMC_{coor.} and DMC_{free} refer to DMC molecules coordinated or uncoordinated

to Na⁺, respectively. **d,** The $A(t)-A(t_0)$ relative absorbance evolution during charging (bottom, blue) and discharging (top, red). The formation of alkyl carbonate (RCOO⁻) is highlighted by a black dotted line at 1,650 cm⁻¹. The relative absorbance of the bands of interest at different wavenumbers during charging are indicated by circles, namely, νC=O of DMC_{free} (red), νC=O of DMC_{coor.} (dark blue), νOCO of DMC_{free} (orange), νOCO of DMC_{coor.} (light blue) and νPF of PF₆⁻ (green). **e,** The $A(t)-A(t_0)$ relative absorbance evolution of the above-mentioned bands during the first charge. Note that prior to conducting operando IR measurements, the background was first collected (I_0) in atmosphere, with the fibre inserted into the cell before filling the electrolyte.

effect on the solvent that is directly visible in the intensity decrease of the νO-C-O and νC-C modes corresponding to coordinated DMC and coordinated EC, and the concomitant increase of those corresponding to free molecules (Fig. 5f). Noteworthy here is the feasibility of observing a change in absorbance that matches the cycling behaviour associated with a repeated change in the concentration of the coordinated cation complexes by switching from charge to discharge (Fig. 5f). By changing the C rate to 1 C, similar observations can be done, confirming the stability of the electrolyte of NaPF₆ in EC/DMC plus 3 wt% VC

(Supplementary Fig. 14). By comparison, this situation was not spotted in the presence of NaPF₆/DMC, as the cell could not be cycled properly (Supplementary Fig. 10).

These results demonstrate that operando IR-FEWS allows for long-standing open questions to finally be answered: What happens when a new additive is mixed with electrolyte? How do different molecules interact with each other in specific voltage ranges? Will a cell be sensitive to resting at a particular state of charge after assembly? Nevertheless, at this stage, a further question arises regarding the

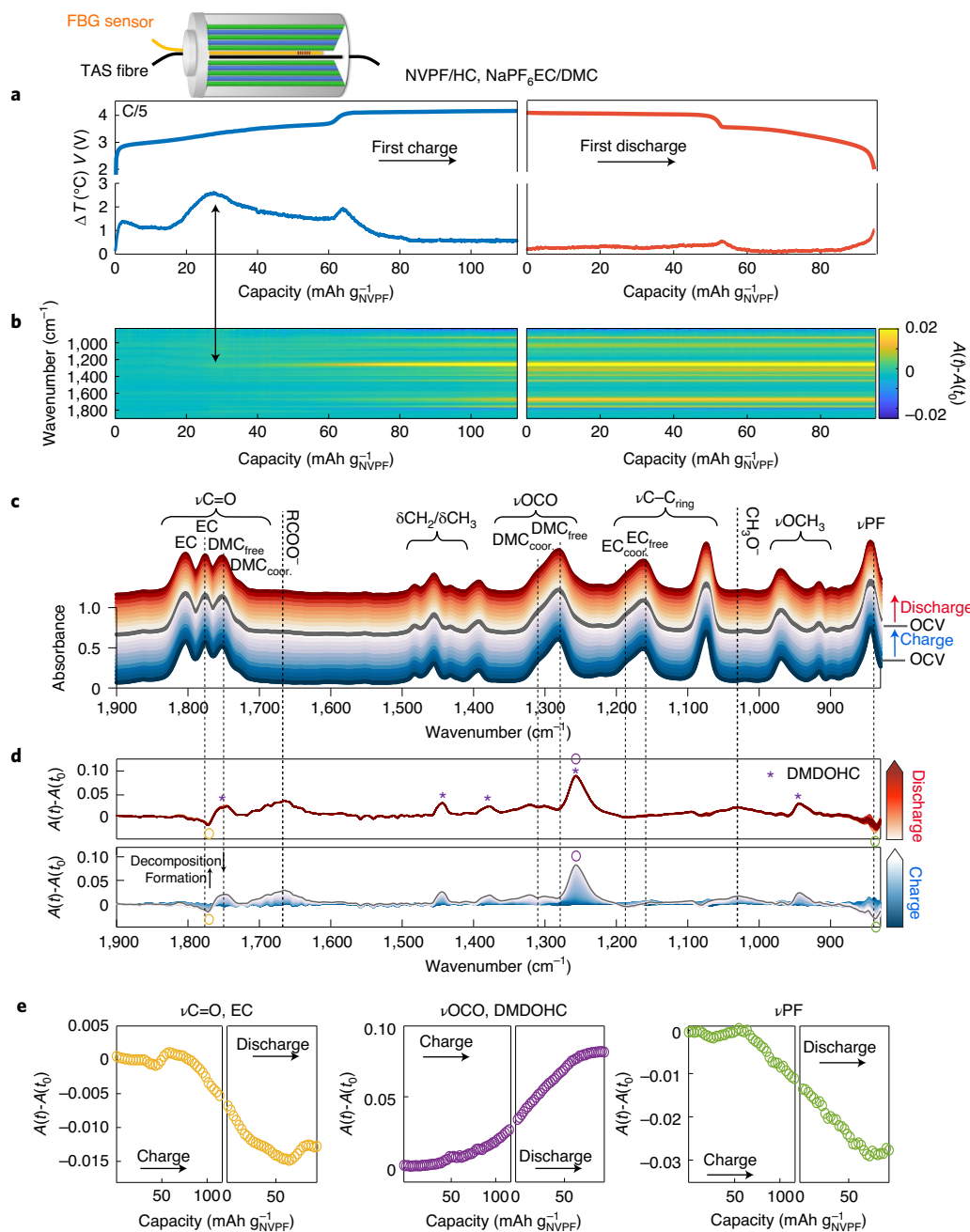


Fig. 4 | Operando IR-FEWS measurements of NaPF₆ in EC/DMC decomposition in 18650. **a**, Schematic drawing of the cell with a FBG sensor and a TAS fibre. Voltage (top) and temperature change (bottom) during the first charge (blue) and discharge (red) of a NVPF/HC 18650 cell with NaPF₆ in EC/DMC electrolyte at C/5. **b**, Wavenumber versus capacity contour plot of $A(t)-A(t_0)$ as a function of capacity. **c**, Absorbance spectra in function of charge (blue) and discharge (red). **d**, The $A(t)-A(t_0)$ relative spectra during charging (bottom, blue) and discharging

(top, red). The formation of DMDOHC, alkyl carbonate (RCOO⁻) and alkoxide (CH₃O⁻) are highlighted by purple stars, the black dotted line at 1,675 cm⁻¹ and the black dotted line at 1,033 cm⁻¹, respectively. The relative absorbance of the bands of interest at different wavenumbers are indicated by circles, namely, ν C=O of EC (yellow), ν OCO of DMDOHC (purple) and ν PF of PF₆⁻ (green). **e**, Evolution of the relative absorbance $A(t)-A(t_0)$ of the above-mentioned bands during the first cycle.

applicability of this method to probing the electrode material itself, since the capability of these fibres may not be limited to liquids.

Embedded and coated fibre

Among electrode materials, we chose to investigate LiFePO₄ (LFP) and Na₃V₂(PO₄)₂F₃ (NVPF), which are both IR active thanks to their PO₄ stretching modes located^{33,34} between 900 cm⁻¹ and 1,200 cm⁻¹, and also commercially relevant today. The former was selected first, as it undergoes a single-step biphasic electrochemical process between two structurally well-defined end members.

Prior to undertaking electrochemical testing, a TAS fibre was coated with LFP, carbon black (CB) and ethanol slurry, then dried prior to being immersed in a solution of I₂ in acetonitrile, which serves as a chemical oxidant (Fig. 6a). The IR spectra collected as a function of time spectacularly reflect the removal of Li according to the reaction $2\text{LiFePO}_4 + \text{I}_2 \rightarrow 2\text{FePO}_4 + 2\text{LiI}$, with the appearance of bands at 1,237 cm⁻¹, 1,095 cm⁻¹ and 951 cm⁻¹ upon delithiation (Fig. 6b,c) similar to those reported for FePO₄³⁵. According to the simulated IR spectra, the lithiated and delithiated compounds have equivalent IR-active modes in the 900–1,300 cm⁻¹ region, therefore

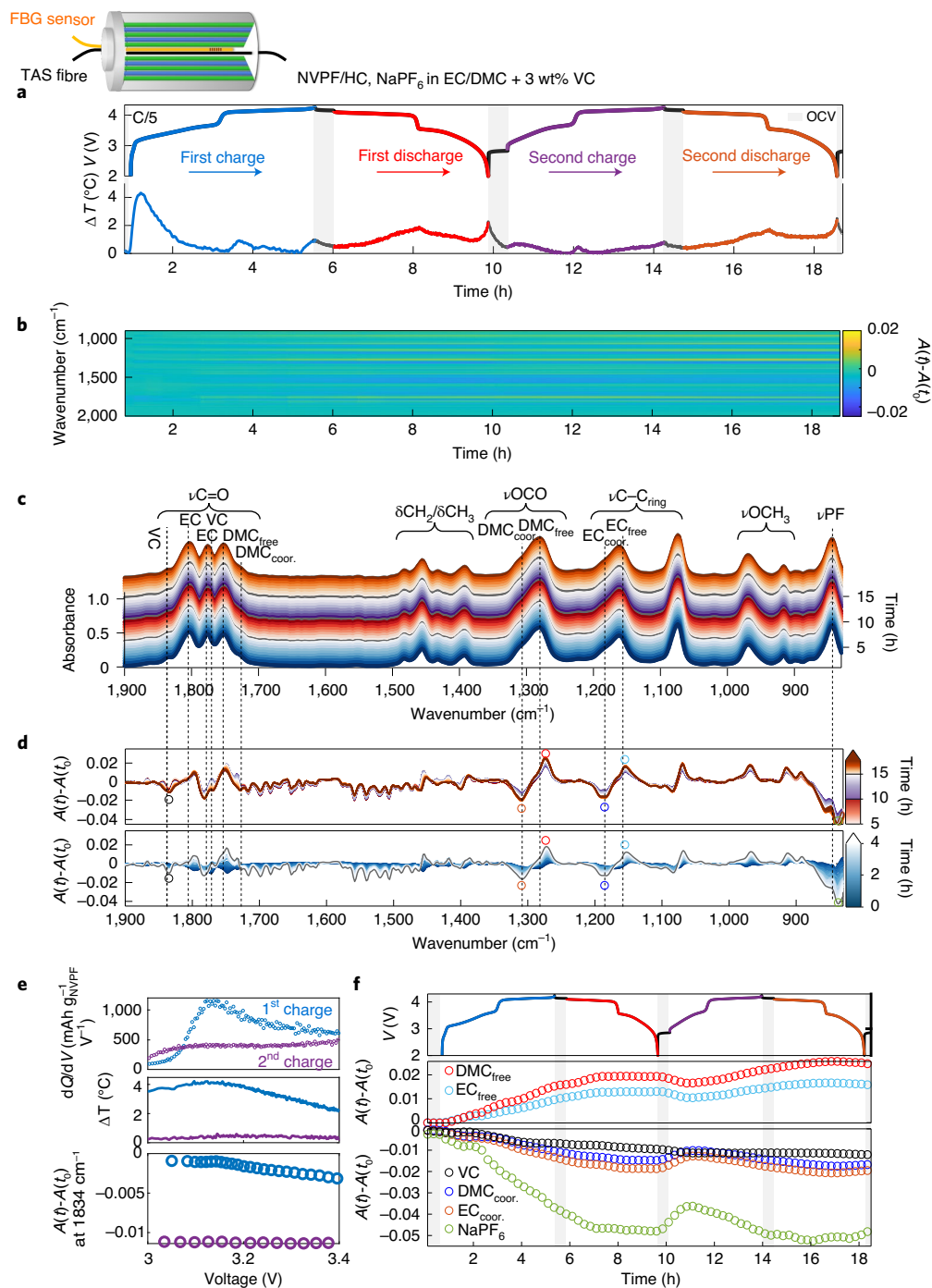


Fig. 5 | Operando IR-FEWS measurements of NaPF₆ in EC/DMC + 3 wt% VC decomposition in 18650. a, Voltage (top) and temperature change (bottom) during the first charge (blue) and discharge (red) and the second charge (purple) and discharge (orange) of a NVPF/HC 18650 cell with NaPF₆ in EC/DMC + 3 wt% VC electrolyte at C/5. **b**, Contour plot of the $A(t)-A(t_0)$ relative absorbance spectra as a function of time. **c**, Absorbance spectra in function of the first charge (blue), first discharge (red), second charge (purple) and second discharge (orange). **d**, The $A(t)-A(t_0)$ relative absorbance spectra during charging (bottom, blue) and discharging (top, red) and the second cycle (top, purple and orange). The bands

of interest at different wavenumbers are indicated by circles, namely, νOCO of free DMC (red) and coordinated DMC (orange), $\nu\text{C}-\text{C}_{\text{ring}}$ of free EC (EC_{free}; light blue) and coordinated EC (EC_{coor.}; dark blue), νPF of PF₆⁻ (green) and $\nu\text{C}=\text{O}$ of VC (black). **e**, Differential capacity dQ/dV as a function of voltage between 3 and 3.5 V (top) and intensity of the band at 1834 cm^{-1} (referenced by the black circle) versus voltage (bottom) during the 1st (blue) and 2nd (purple) charge. **f**, The $A(t)-A(t_0)$ relative evolution of the above-mentioned bands during the first two cycles, plotted versus time.

allowing a one-to-one correspondence of each mode, detailed in Supplementary Fig. 15. Thanks to this complete band assignment, the lithium extraction can be followed over time, providing new information on the reaction kinetics of LFP with I₂ (Supplementary Fig. 16).

Next, a TAS fibre was embedded in the mixture of LFP and CB and used as the positive electrode in a Li half-cell (Fig. 6d) using 1 M LiPF₆ in DMC as an electrolyte since its IR bands do not overlap with those of LiFePO₄ (Supplementary Fig. 17). Upon charging, the voltage profile yields a plateau at 3.6 V, characteristic of the biphasic mechanism

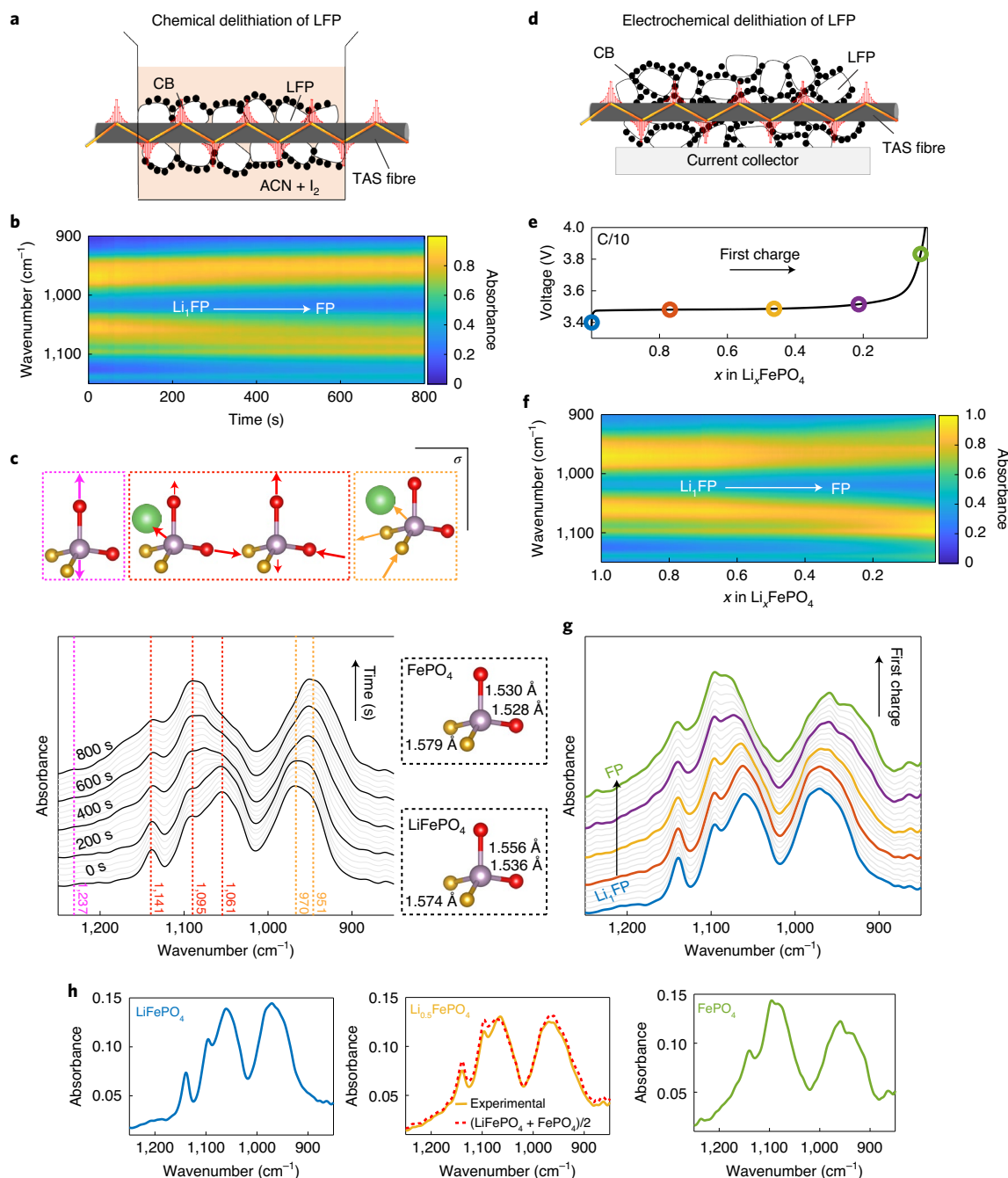


Fig. 6 | Operando IR-FEWS measurement of fibre coated and embedded in LFP. **a**, Schematic drawing of fibre coated with LFP + CB. The material is immersed at $t = 0$ s in a solution of acetonitrile (ACN) and iodine (I_2) in order to chemically delithiate the material. **b**, Contour plot of the absorbance spectra in the 800–1,150 cm^{-1} region as a function of time. **c**, Stacked absorbance spectra (bottom) of the coated fibre at 0 s, 200 s, 400 s, 600 s and 800 s. The PO_4 local structures of LiFePO_4 and FePO_4 are shown at the right. For the olivine structure ($\text{LiFePO}_4/\text{FePO}_4$), two oxygen atoms (orange) share an edge with one FeO_6 octahedra and the two other ones (red) share a corner with two different FeO_6 octahedra. The vibration modes are indicated at the top of the figure.

d, Schematic drawing of the fibre embedded in an electrode of LFP + CB. **e**, First charge of LFP/Li cell with 1 M LiPF_6 in DMC as an electrolyte at C/10 up to 4 V. For an easy follow-up of the band evolution, circles have been added on the voltage profile and kept in the infrared spectra. **f**, Contour plot of the absorbance IR-FEWS spectra in the 800–1,150 cm^{-1} region as a function of the lithium content x in Li_xFePO_4 . **g**, Stacked IR-FEWS absorbance spectra at different values of the lithium content x . **h**, IR-FEWS absorbance spectra of LiFePO_4 , $\text{Li}_{0.5}\text{FePO}_4$ and FePO_4 obtained in operando by electrochemical delithiation, and the calculated $\text{Li}_{0.5}\text{FePO}_4$ spectra (dashed line), calculated using the average spectra of the two phases.

between LiFePO_4 and FePO_4 (Fig. 6e and Supplementary Fig. 17a). As observed in Fig. 6f,g, the IR spectra recorded upon cycling exhibit progressive modification of the νPO_4 bands, similar to the change previously obtained with chemical oxidation (as well as ex situ measurements provided in Supplementary Fig. 17c). Interestingly, the band

evolution confirms the biphasic delithiation mechanism of LFP, with the intermediate spectra being a mixture of LiFePO_4 and FePO_4 spectra (an example for $\text{Li}_{0.5}\text{FePO}_4$ is given in Fig. 6h). During discharge, the spectra reverse back to that of the pristine material (full cycle information is provided in Supplementary Fig. 18), clearly showing the

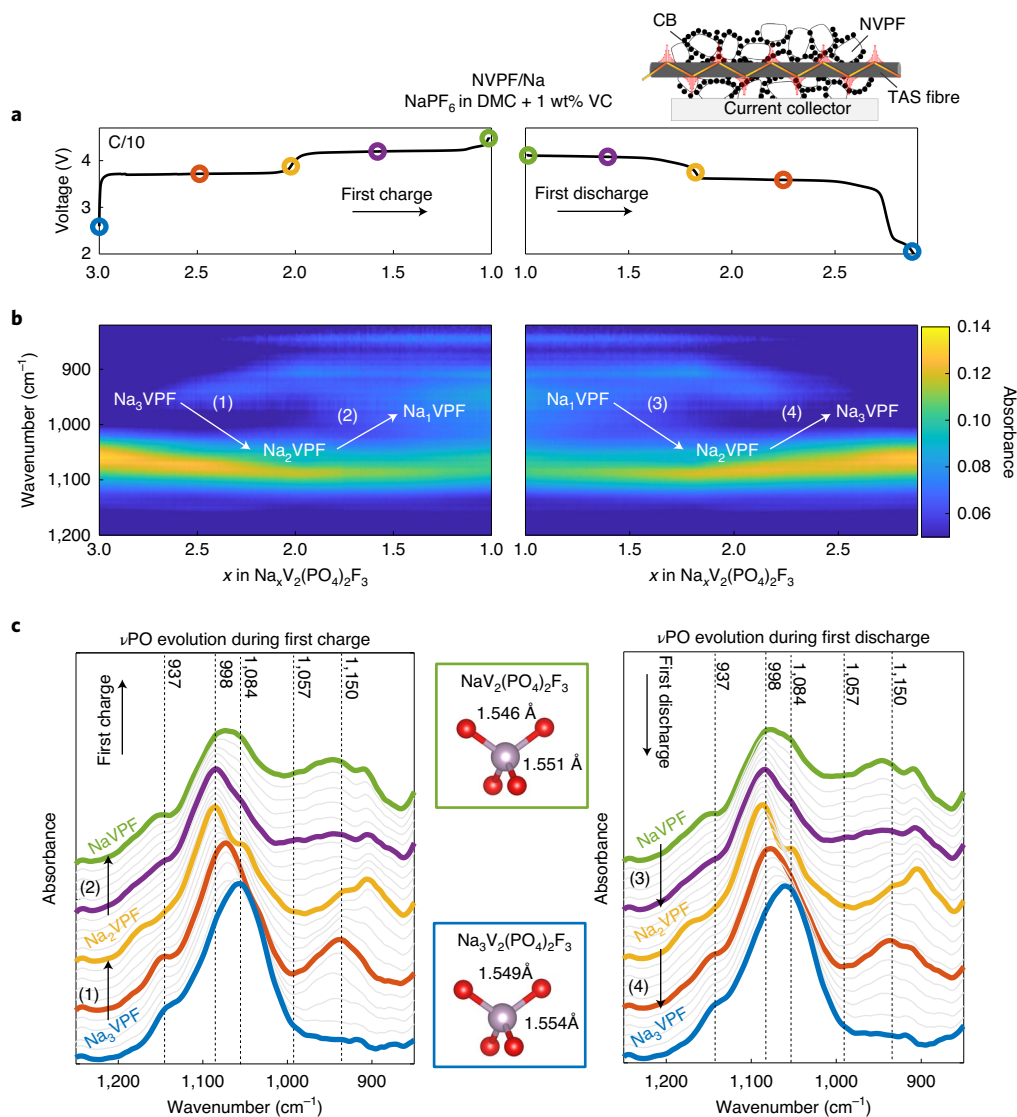


Fig. 7 | Operando IR-FEWS measurement of fibre embedded in NVPF.

a, Schematic drawing of the experiment (top) and the voltage profile as a function of the sodium content x in $\text{Na}_x\text{V}_2(\text{PO}_4)_2\text{F}_3$ during the first cycle of the NVPF/Na cell with $\text{NaPF}_6/\text{DMC} + 1 \text{ wt\% VC}$ as electrolyte at C/10 between 2 and 4.5 V. For an easy follow-up of the band evolution, circles have been added on the voltage profile and kept in the infrared spectra. **b**, Contour plot of the absorbance spectra in the 850–1,200 cm^{-1} region as a function of the sodium content x during the first cycle. **c**, Stacked absorbance spectra in the 850–1,200 cm^{-1} region at different values of the sodium content x that match the coloured circles in the voltage curve, during the first charge (left) and the first discharge (right). The

spectral changes observed around 850 cm^{-1} for the first cycle of NVPF with embedded fibre are incongruent with those observed previously and attributed to vPF. This underscores the power of the IR-FEWS approach, as opposed to being an inconsistency. In each case, measurements are spatially localized to such an extent that the same spectral regions can be used to observe different physio-chemical phenomena (for example, either in the electrolyte or in the electrode material) without the need for complex decoupling approaches. The PO_4 local structures of Na_3VPF and Na_1VPF are shown in the blue and green panels, respectively (Supplementary Fig. 15 for calculated spectra and vibrations).

feasibility of tracking Li intercalation and de-intercalation processes in operando and thereby enabling us to track the Li inventory during cycling and to access the cell's state of charge (Supplementary Fig. 19). As a means of simplification, we demonstrate that similar results can be obtained using a fibre coated with LFP and CB and tested in the same electrochemical conditions (full cycle information is provided in Supplementary Fig. 20).

A TAS fibre embedded in a mixture of NVPF and CB was then used to track the Na uptake–removal in NVPF, which is known to undergo a multi-step electrochemical mechanism associated with phase transformations³⁶. A Na/NVPF half-cell was assembled and cycled with 1 M NaPF_6 in DMC plus 1 wt% of VC as an electrolyte; two plateaus become evident at 3.7 V and 4.2 V, corresponding to the extraction of two sodium ions,

from Na_3VPF to Na_2VPF and from Na_2VPF to Na_1VPF , respectively (Fig. 7a). The de-intercalation of sodium in Na_3VPF has been reported as a four-step mechanism, including two different biphasic regions in the first plateau followed by one solid solution and one biphasic region in the second plateau³⁶. The IR spectra corroborate this mechanism with the appearance of a band first at 937 cm^{-1} , followed by another one at 1,084 cm^{-1} during the first Na removal. During the second Na removal, the broad bands at 998 and 937 cm^{-1} (Fig. 7b,c) are observed to grow, while the band at 1,084 cm^{-1} shifts. The simulated IR spectra shown in Supplementary Fig. 15 confirm the appearance of two new IR-active modes for the Na_1VPF (with sodium removed) in the 900–1,000 cm^{-1} region, which are assigned to the vibration of the Na cages, and other PO_4 bands that are common to Na_3VPF and Na_1VPF . All these bands

convert back to their initial positions on the subsequent discharge, with the pre-charge spectrum being nearly identical to the post-discharge spectrum. Simultaneously, we spot only slight changes in the solvent absorption bands due to the dynamics of Na during intercalation and de-intercalation, as well as the decomposition of the electrolyte (Supplementary Fig. 21), further highlighting the sensitivity of the technique. Lastly, IR optical detection can also be used to track the Li(Na) uptake–removal process in organic electrodes (Supplementary Fig. 22).

Altogether, the findings indicate that this approach is capable of following the intercalation and de-intercalation processes of Li(Na) in battery materials and high-carbon-content composite electrodes, thereby circumventing the limitations of conventional attenuated total reflectance spectroscopy. Moreover, we were able to follow the decomposition of the electrolyte and the dynamics of the solvent within the same experiment, hence underscoring another advantage of operando IR-FEWS, since electrode and electrolyte interactions will always be interlinked and codependent on each other.

Conclusions

We have introduced an operando optical-fibre-based evanescent wave infrared spectroscopy relying on benign chalcogenide fibres for monitoring the evolving chemistry in commercial 18650 Na-ion batteries under real working conditions, which is a long-standing dream within the field of battery sensing. We demonstrate the validity of our technique by surveying the respective stability of electrolytes with various compositions of solvents or additives. We successfully revealed changes in the dynamics of these solvents and additives without any latency, which enables us to identify the nature of the electrolyte decomposition species with excellent sensitivity as well as changes in the ion solvation dynamics as a function of the voltage and current. Through our study, we could verify the greatest instability of 1 M NaPF₆ electrolytes based on DMC versus EC–DMC or EC–DMC–VC and similarly confirm the proposed decomposition mechanism that took years of conventional lab work to establish. Furthermore, we have shown the ability to track the potential at which a popular electrolyte additive, VC, is electrochemically reduced to stabilize the reduction of EC/DMC.

The in-depth assessment of this chemistry at the molecular level in the first formation cycle after cell manufacturing and onward can be of great value to battery manufacturers, since this formation step is the ‘trade secret’ for each company. The lack of any real-time diagnostic technique means that even in today’s best Li-ion cells, the routine for SEI formation is established by trial-and-error approaches. While any new information regarding the selection of cell currents and cell potentials during formation is helpful, unique identification of the molecular species participating in SEI nucleation and growth can translate into a new era for extending battery life.

In addition to the detection of the electrolyte, we proved the feasibility of following the Li uptake–removal process in carbon composite electrode materials by monitoring the IR-active modes of the P–O bond for LFP and NVPF, and the C=O bond for the Li-terephthalate, bearing in mind that carbon is usually not a friendly element for IR spectroscopy. We can readily envision extending this study to other inorganic compounds like V₂O₅, LiMnO₂ and LiCoO₂, or to Li-rich transition metal oxides undergoing still unclear O–O bond reorganization upon cycling, provided that we slightly enlarge the transmittance window of the chalcogenide fibre. This calls for a deeper exploration of the chalcogenide glass design space to enable the probing of larger IR windows, in particular probing the M–O IR bands, which are usually located around 16 μ m.

Although we stress the added fundamental insights that IR-FEWS can offer to the battery community regarding the nature of the pertinent chemistries and molecular species, we are not yet offering a novel turnkey diagnostic technology. Nevertheless, we envision immediate use from the preliminary experimentation, regarding

either formation cycle strategies or guidance for handling and storage as a function of state of charge and temperature. Turning to use in the field, although the fibres are insulating and chemically stable, there are several engineering limitations dealing with the brittleness of TAS fibres and the engineering of apertures in the cell. Such designs must avoid perturbing the venting valve and affirm airtightness, in the absence of any effect on long-term performance (beyond the 100 cycles we have tried here). Additionally, different decomposition and formation reactions can induce counteractive effects on the infrared signal, hence making the deconvolution of the spectra complex without advanced data treatments. Methods based on machine learning could be one route to explore in order to quantify the different solvents during operando measurements^{19–21}. Nevertheless, encouraging progress is already being made by the company DIAFIR, which uses fibre-based IR spectroscopy for medical diagnosis^{19,20}, and thus solutions for some complications might be found from synergistic efforts in other domains.

Lastly, we limited our concept demonstration to non-microstructured fibres, but we envision the same type of experiment with hollow core fibres drastically increasing the evanescent field penetration and enhancing the sensitivity for IR detection. Compared to FBG sensing, one disadvantage of IR-FEWS is that we cannot host multiple distinct sensors in a single fibre segment, and we do not have multi-channel spectrometers, thus losing the multiplexing advantage. However, ongoing studies are already utilizing the relatively quick spectrum acquisition time of IR-FEWS in combination with optical switches to enable a single IR channel to periodically monitor multiple fibres, hence enabling ageing studies and identification of ageing mechanisms. One scenario we envision in the field is to have a single battery module equipped with an IR-FEWS sensor, while the other modules in the pack could be considered as twins and thus be without the diagnostic hardware.

With the demonstration here of in operando IR spectroscopy via optical TAS fibres, we see unprecedented opportunities for improved battery diagnostics under real working conditions. It is our hope that this technique opens what has long been considered a black box (chemistry-wise) to new insights that will rapidly enable the battery community to conquer challenges with formulating new electrolytes and optimizing battery formation protocols that govern battery lifetime and inevitably, their environmental impact.

Methods

Cell and electrode preparation

The 18650 NVPF/HC cells were provided dried and hermetically sealed without electrolyte by Tiamat. To test the inertness of the TAS fibre, a single 0.8 mm hole was drilled in the centre of the negative pole of the cell. The electrolyte was then injected in an argon-filled glove box (<0.1 ppm H₂O and O₂) and the hole was closed with epoxy that cured for 12 h. For the fibre embedded in the electrode, the active material powder LFP (Umicore) and NVPF (made via a two-step ceramic process³⁷) were ground for ~10 minutes in a mortar with 10 wt% CB Super P (TIMCAL, Alfa Aesar) as a conductive agent. Next, a few droplets of ethanol were added to the powder, and the slurry was placed on the fibre. For all the materials, the current collector was stainless steel with a diameter of 19 mm. All electrodes were dried overnight in a vacuum oven at 80 °C before transfer into the glove box.

Electrolyte preparation

In this work, the different sodium-based electrolytes used NaPF₆ (Stella Chemica) as the salt. The formulations were 1 M NaPF₆ in DMC (E-lyte, anhydrous, >99%), 1 M NaPF₆ in EC/DMC (1:1, v/v; EC from Mitsubishi Chemical) and 1 M NaPF₆ in EC/DMC + 3 wt% VC (Tinci). For the lithium-ion cell, the electrolyte prepared is 1 M LiPF₆ (solvionic) in DMC + 1 wt% of VC (Tinci). The 1 M LiPF₆ in EC/DMC (LP30) has been provided by E-lyte.

Integration of fibres into the modified Swagelok for reference acquisition

The Swagelok cell (diameter = 13 mm) was drilled with two holes of 0.45 mm for the fibre to pass through, and two metal tubes terminated with rubber septa were welded to the cell body to inject and evacuate the electrolyte while maintaining the inert atmosphere inside the cell core while adding and removing solutions. Then an ~50-cm-long TAS fibre was passed through the cell, attached on both external sides with epoxy and cured for 12 h. The cell was closed in the glove box, then taken out and attached to the spectrometer and detector, and the air-sensitive solutions were injected using syringes also prepared in the glove box.

Integration of fibres into the 18650 cells

The 18650 cells were drilled with two holes of 0.8 mm on the centre of the negative and positive sides of the cell to allow the fibre to pass through the central void of the jelly roll. The drilled cells were dried under vacuum overnight at 80 °C and introduced into the argon-filled glove box. Using a needle (diameter = 0.45 mm) as a guide, a TAS fibre with a length of about 50 cm was passed through the cell. Once the fibre was placed with approximately the same length of fibre going out from each part of the cell, the hole on the positive electrode side was closed with epoxy and cured for 12 h. Then, the fibre was connected to the spectrometer for background acquisition. Finally, in the glove box, about 5.3 ml of electrolyte was injected from the hole on the negative side, and this hole was also sealed with epoxy and cured for 12 h. The cell was again connected to the spectrometer to acquire the infrared spectra. In post-processing, the contribution of the epoxy to the infrared spectra was subtracted, allowing one to see only the variations in the electrolyte.

Fibre embedded/coated into the electrode

The body of a Swagelok cell was drilled from side to side (diameter = 19 mm), and a stainless steel current collector was used to apply the electrode slurry. The stainless steel plunger and current collector were aligned with the holes in the cell body so that the fibre would pass through the hole on top of the current collector. The fibre was fixed on both sides with cured epoxy for 12 hours and connected to the spectrometer once to acquire a background. Then, a droplet of the electrode formulation was deposited and spread on the surface of the fibre and the current collector. The entire assembly was finally dried overnight at 80 °C in a vacuum oven.

In a glove box, the cells were assembled with two glass fibre separators (GF/D, Whatman) and a disc of lithium metal for the LFP electrode and sodium metal for the NVPF electrode.

For the coating, the fibre was first immersed for a few seconds in a slurry and air dried without contact on the previously immersed part. Then the fibre was passed through the cell and fixed with epoxy. The rest of the experiment proceeded as before.

IR-FEWS operando measurements

The operando measurements were performed with a Fourier-transformed infrared spectrometer (T37 or Invenio S, Bruker) with an accessory connection system on the right side to focus the infrared beam on one entry extremity of the fibre. A mercury–cadmium–tellurium detector with a spectral range of 12,000–600 cm^{-1} was used to record the optical signal at the output extremity of the fibre. During all the experiments, the mercury–cadmium–tellurium detector was cooled with liquid nitrogen. For all the experiments, the edges of the TAS fibre were cleaved manually. First, the fibre was marked perpendicular to the axis with a scalpel blade. Then, the fibre was pulled apart to produce a clean break. Finally, the edge was inspected with a fibre inspection scope (Thorlabs). The edge had to be flat, perpendicular and clean to have the beam going through the fibre with minimal loss. Then, using a bare fibre terminator and multimode connectors, the fibres were attached to the light source and the detector. The signal between the input and output of the fibre was controlled, with an

amplitude around 10,000 for 150 μm TAS fibre. The IR-FEWS spectra were acquired with 16 scans and a resolution of 4 cm^{-1} for a total acquisition time of 4 seconds. The spectra were recorded every 120 seconds during all the electrochemical tests. Note that the recording between the spectra was set at 120 seconds because it was not necessary to have more spectra at the C rates used in this study. To minimize the atmospheric variations that directly affect part of the fibre outside the cell and the background, a tight Plexiglas box was used to protect the whole set-up. Due to this, a change in water absorbance of only 0.0004 was observed after 24 hours of measurements (Supplementary Fig. 23).

Optical measurements with FBG

The FBGs used in the study were provided by Samyon and are 6 mm long, with a Bragg wavelength centred around 1,555 nm. The optical signals were acquired by an FBGuard1550 (Safibra) interrogator, with a wavelength accuracy/resolution of 1 pm.

Calibration of FBG sensors

The temperature calibration of the FBG sensors was conducted in the temperature ovens (IPP55, Mermmet) from 35 to 15 °C in 5 °C increments and 4 h steps.

Electrochemical tests

Electrochemical properties were evaluated at room temperature by SP50 or MPG2 potentiostat (Biologic). The C rate was calculated using the mass of active material of the positive electrode. The ICs of NVPF and LFP are 128 and 170 mA g^{-1} , respectively. The voltage window for NVPF/HC was 2.0–4.5 V, for NVPF/Na was 2.0–4.5 V and for LFP/Li was 3.0–4.0 V.

Chemical delithiation

The chemical delithiation was realized using a solution of iodine (99+%, Alfa Aesar) in acetonitrile (Sigma-Aldrich). The amount of iodine was calculated to be in excess compared to LFP.

Computational details

Calculations were performed using the CRYSTAL17 code^{38–41} with all-electron atomic basis sets and the B3LYP functional for the exchange and correlation potential. Gaussian basis sets of 6–11G, 86–411d41G, 85–21d1G, 8–511G, 86–411d4G, 8–411G and 7–311 were employed to describe the Li, Fe, P, Na, V, O and F atoms. All atom coordinates and lattice parameters were fully relaxed using conjugate gradient energy minimization, and the force tolerance for structural relaxation was set to 2.10–5 eV Å^{-1} . Vibrational frequencies were calculated within the harmonic approximation, and the IR intensities were calculated using the CPKS method^{42,43}.

Data availability

The datasets generated during the current study are available in the article and its Supplementary Information.

References

1. Larcher, D. & Tarascon, J.-M. Towards greener and more sustainable batteries for electrical energy storage. *Nat. Chem.* **7**, 19–29 (2015).
2. Wang, F. et al. Tracking lithium transport and electrochemical reactions in nanoparticles. *Nat. Commun.* **3**, 1201 (2012).
3. Blanc, F., Leskes, M. & Grey, C. P. *In situ* solid-state NMR spectroscopy of electrochemical cells: batteries, supercapacitors, and fuel cells. *Acc. Chem. Res.* **46**, 1952–1963 (2013).
4. Zhang, Y. et al. Revealing electrolyte oxidation *via* carbonate dehydrogenation on Ni-based oxides in Li-ion batteries by *in situ* Fourier transform infrared spectroscopy. *Energy Environ. Sci.* **13**, 183–199 (2020).

5. Sathiyaraj, M. et al. Electron paramagnetic resonance imaging for real-time monitoring of Li-ion batteries. *Nat. Commun.* **6**, 6276 (2015).
6. Grey, C. P. & Tarascon, J. M. Sustainability and in situ monitoring in battery development. *Nat. Mater.* **16**, 45–56 (2016).
7. Huang, J., Boles, S. T. & Tarascon, J.-M. Sensing as the key to battery lifetime and sustainability. *Nat. Sustain.* **5**, 194–204 (2022).
8. Peng, J. et al. High precision strain monitoring for lithium ion batteries based on fiber Bragg grating sensors. *J. Power Sources* **433**, 226692 (2019).
9. Sommer, L. W. et al. Embedded fiber optic sensing for accurate state estimation in advanced battery management systems. *MRS Online Proc. Libr.* **1681**, 1–7 (2014).
10. Huang, J. et al. Operando decoding of chemical and thermal events in commercial Na(Li)-ion cells via optical sensors. *Nat. Energy* **5**, 674–683 (2020).
11. Desai, P. et al. Deciphering interfacial reactions via optical sensing to tune the interphase chemistry for optimized Na-ion electrolyte formulation. *Adv. Energy Mater.* **11**, 2101490 (2021).
12. Huang, J. et al. Monitoring battery electrolyte chemistry via in-operando tilted fiber Bragg grating sensors. *Energy Environ. Sci.* <https://doi.org/10.1039/D1EE02186A> (2021).
13. Manap, H., Dooly, G., O’Keeffe, S. & Lewis, E. Ammonia detection in the UV region using an optical fiber sensor. *Sens. 2009 IEEE* <https://doi.org/10.1109/ICSENS.2009.5398215> (2009).
14. Michel, K. et al. Monitoring of pollutant in waste water by infrared spectroscopy using chalcogenide glass optical fibers. *Sens. Actuators B Chem.* **101**, 252–259 (2004).
15. Yan, D., Popp, J., Pletz, M. W. & Frosch, T. Highly sensitive broadband Raman sensing of antibiotics in step-index hollow-core photonic crystal fibers. *ACS Photonics* **4**, 138–145 (2017).
16. Cubillas, A. M. et al. Photonic crystal fibres for chemical sensing and photochemistry. *Chem. Soc. Rev.* **42**, 8629–8648 (2013).
17. Bertucci, A. et al. Detection of unamplified genomic DNA by a PNA-based microstructured optical fiber (MOF) Bragg-grating optofluidic system. *Biosens. Bioelectron.* **63**, 248–254 (2015).
18. Miele, E. et al. Hollow-core optical fibre sensors for operando Raman spectroscopy investigation of Li-ion battery liquid electrolytes. *Nat. Commun.* **13**, 1651 (2022).
19. Ellis, L. D. et al. A new method for determining the concentration of electrolyte components in lithium-ion cells, using Fourier transform infrared spectroscopy and machine learning. *J. Electrochem. Soc.* **165**, A256–A262 (2018).
20. Buteau, S. & Dahn, J. R. Analysis of thousands of electrochemical impedance spectra of lithium-ion cells through a machine learning inverse model. *J. Electrochem. Soc.* **166**, A1611–A1622 (2019).
21. Corvec, M. L. et al. Fast and non-invasive medical diagnostic using mid infrared sensor: the AMNIFIR project. *Innov. Res. Biomed. Eng.* **37**, 116–123 (2016).
22. Calvez, L. Chalcogenide glasses and glass-ceramics: transparent materials in the infrared for dual applications. *Comptes Rendus Phys.* **18**, 314–322 (2017).
23. Cresce, A. V. et al. Solvation behavior of carbonate-based electrolytes in sodium ion batteries. *Phys. Chem. Chem. Phys.* **19**, 574–586 (2016).
24. Yan, G. et al. A new electrolyte formulation for securing high temperature cycling and storage performances of Na-ion batteries. *Adv. Energy Mater.* **9**, 1901431 (2019).
25. Eshetu, G. G. et al. Comprehensive insights into the reactivity of electrolytes based on sodium ions. *ChemSusChem* **9**, 462–471 (2016).
26. Yan, G. et al. Assessment of the electrochemical stability of carbonate-based electrolytes in Na-ion batteries. *J. Electrochem. Soc.* **165**, A1222 (2018).
27. Angell, C. L. The infra-red spectra and structure of ethylene carbonate. *Trans. Faraday Soc.* **52**, 1178 (1956).
28. Yoshida, H. et al. Degradation mechanism of alkyl carbonate solvents used in lithium-ion cells during initial charging. *J. Power Sources* **68**, 311–315 (1997).
29. Nyquist, R. A. & Settineri, S. E. Infrared study of ethylene carbonate in various solvents and solvent systems. *Appl. Spectrosc.* **45**, 1075–1084 (1991).
30. Pan, Y. et al. Investigation of the solid electrolyte interphase on hard carbon electrode for sodium ion batteries. *J. Electroanal. Chem.* **799**, 181–186 (2017).
31. Aurbach, D. et al. On the use of vinylene carbonate (VC) as an additive to electrolyte solutions for Li-ion batteries. *Electrochim. Acta* **47**, 1423–1439 (2002).
32. Sasaki, T., Abe, T., Iriyama, Y., Inaba, M. & Ogumi, Z. Suppression of an alkyl dicarbonate formation in Li-ion cells. *J. Electrochem. Soc.* **152**, A2046 (2005).
33. Kosova, N. V. & Rezapova, D. O. Na_{1+y}VPO₄F_{1+y} (0 ≤ y ≤ 0.5) as cathode materials for hybrid Na/Li batteries. *Inorganics* **5**, 19 (2017).
34. Boivin, É. Crystal chemistry of vanadium phosphates as positive electrode materials for Li-ion and Na-ion batteries. <https://tel.archives-ouvertes.fr/tel-03648931> (2017).
35. Ait Salah, A. et al. FTIR features of lithium-iron phosphates as electrode materials for rechargeable lithium batteries. *Spectrochim. Acta A Mol. Biomol. Spectrosc.* **65**, 1007–1013 (2006).
36. Bianchini, M. et al. Comprehensive investigation of the Na₃V₂(PO₄)₂F₃–NaV₂(PO₄)₂F₃ system by operando high resolution synchrotron X-ray diffraction. *Chem. Mater.* **27**, 3009–3020 (2015).
37. Bianchini, M. et al. Na₃V₂(PO₄)₂F₃ revisited: a high-resolution diffraction study. *Chem. Mater.* **26**, 4238–4247 (2014).
38. Becke, A. D. A new mixing of Hartree–Fock and local density-functional theories. *J. Chem. Phys.* **98**, 1372–1377 (1993).
39. Lee, C., Yang, W. & Parr, R. G. Development of the Colle–Salvetti correlation-energy formula into a functional of the electron density. *Phys. Rev. B* **37**, 785–789 (1988).
40. Erba, A., Baima, J., Bush, I., Orlando, R. & Dovesi, R. Large-scale condensed matter DFT simulations: performance and capabilities of the CRYSTAL code. *J. Chem. Theory Comput.* **13**, 5019–5027 (2017).
41. Dovesi, R. et al. Quantum-mechanical condensed matter simulations with CRYSTAL. *WIREs Comput. Mol. Sci.* **8**, e1360 (2018).
42. Maschio, L., Kirtman, B., Rérat, M., Orlando, R. & Dovesi, R. *Ab initio* analytical Raman intensities for periodic systems through a coupled perturbed Hartree–Fock/Kohn–Sham method in an atomic orbital basis. I. Theory. *J. Chem. Phys.* **139**, 164101 (2013).
43. Maschio, L., Kirtman, B., Rérat, M., Orlando, R. & Dovesi, R. *Ab initio* analytical Raman intensities for periodic systems through a coupled perturbed Hartree–Fock/Kohn–Sham method in an atomic orbital basis. II. Validation and comparison with experiments. *J. Chem. Phys.* **139**, 164102 (2013).

Acknowledgements

J.-M.T. acknowledges the International Balzan Prize Foundation and the LABEX STOREXII for funding. C.G.-M. and J.-M.T. acknowledge Bruker for the instrumental set-up. We thank Tiamat for providing the NVPF/HC 18650 cells and R. Dugas for his assistance in the cell fabrication. We thank R. Chometon for the scanning electron microscopy images. M.B.Y. acknowledges the support of the French Agence Nationale de la Recherche (ANR) under reference ANR-

17-CE05-10 (project VASELinA). S.T.B. acknowledges the support from the ENERSENSE research initiative (68024013) at the Norwegian University of Science and Technology (NTNU), Norway. Finally, we gladly thank S. Mariyappan, P. Desai and D. Larcher for valuable discussions and comments.

Author contributions

C.G.-M. and J.-M.T. conceived the idea and designed the experiments with the help of C.B.-P., J.L.A. and X.H.Z., who provided the adequate fibre. C.G.-M. performed the electrochemical tests, optical tests and data analysis. M.B.Y. and M.-L.D. conducted the theoretical analysis. C.B.-P., J.H., L.A.B., S.T.B., C.L., X.H.Z., J.L.A. and J.-M.T. conjointly discussed the data and their meaning. Finally, C.G.-M., M.-L.D. and J.-M.T. wrote the paper, with contributions from all authors.

Competing interests

A patent related to the work has been submitted (application no. PCT/EP2022/071395) by the Centre National de la Recherche Scientifique, Collège de France, Sorbonne Université, Université de Rennes 1, Ecole Nationale Supérieure de Chimie de Rennes and Institut National des Sciences Appliquées de Rennes. The inventors are Jean-Marie Tarasco, Charlotte Gervillié, Catherine Boussard, Xiang-Hua Zhang and Jean-Luc Adam. The patent covers a method for operando characterization of chemical species within a battery using infrared fibre evanescent wave spectroscopy.

Additional information

Supplementary information The online version contains supplementary material available at <https://doi.org/10.1038/s41560-022-01141-3>.

Correspondence and requests for materials should be addressed to J.-M. Tarascon.

Peer review information *Nature Energy* thanks Yifei Yu and the other, anonymous, reviewer(s) for their contribution to the peer review of this work.

Reprints and permissions information is available at www.nature.com/reprints.

Publisher's note Springer Nature remains neutral with regard to jurisdictional claims in published maps and institutional affiliations.

Springer Nature or its licensor (e.g. a society or other partner) holds exclusive rights to this article under a publishing agreement with the author(s) or other rightsholder(s); author self-archiving of the accepted manuscript version of this article is solely governed by the terms of such publishing agreement and applicable law.

© The Author(s), under exclusive licence to Springer Nature Limited 2022